Are Early Triassic extinction events associated with mercury anomalies? A reassessment of the Smithian/Spathian boundary extinction

Øyvind Hammer[1], Morgan T. Jones[2], Elke Schneebeli-Hermann[3], Bitten Bolvig Hansen[1], Hugo Bucher[3]

[1] Natural History Museum, University of Oslo, Pb. 1172 Blindern, 0318 Oslo, Norway

[2] Centre for Earth Evolution and Dynamics (CEED), Pb. 1028 Blindern, 0315 Oslo, Norway

[3]Paläontologisches Institut und Museum, Universität Zürich, Karl-Schmid-Strasse 4, 8006 Zürich, Switzerland

Abstract

High concentrations of mercury, possibly connected with widespread volcanism of the Siberian Traps, have previously been associated with the Smithian/Spathian (Early Triassic) boundary (SSB) in the Sverdrup Basin, Tethyan sections in India and China, as well as with a shallow-water record in western Spitsbergen. We confirm this Hg/TOC anomaly in the deeper water record at Wallenbergfjellet, central Spitsbergen. However, both paleontological age control and carbon isotopes indicate that the Hg anomaly occurred mainly within strata of middle Smithian age. Therefore, this Hg anomaly is unlikely to be directly causally related to mechanisms contributing to the late Smithian global extinction of nektonic faunas. The TOC and trace element data suggest generally more oxygenated conditions during the Smithian compared to the Spathian, which is at odds with the hypothesis that oxygen depletion may have been a global kill mechanism for the SSB extinction. Further work is needed to assess if precise timing and paleogeographic distribution of anoxia shows any consistent pattern or not during the Smithian and Spathian. The very abrupt lower limb of the positive carbon isotope excursion (CIE) and the coarser grain size immediately below the boundary between the Lusitaniadalen Member and the Vendomdalen Member indicate a substantial stratigraphic gap of latest Smithian age, a previously neglected signal shared with many other boreal SSB sections. Ammonoid age control also indicates that the onset of the late Smithian gap in the high

latitudes was earlier than in the Tropics. The gradual end of the positive CIE contrasts with the frequent spike shape observed in tropical shelf records and is definitively earliest Spathian in age. The middle Smithian Hg anomaly in the Boreal record is only visible in the Hg/TOC values, and is associated with a possible shift in organic matter type from terrestrial to marine in the case of Spitsbergen. This suggests that the middle Smithian Hg/TOC anomaly in Spitsbergen may not unequivocally originate from volcanism, and calls for additional caution before interpreting Hg spikes as a volcanic proxy.

Key words: Earth crises; volcanism; extinction; carbon isotopes; Spitsbergen

Outline:

1. Introduction

The Early Triassic is a fascinating epoch in Earth history, as ecosystems rebuilt and reformed in the aftermath of the end-Permian extinction event, the most biologically severe mass extinction in the Phanerozoic (Sepkoski, 1996; 2002). The most commonly cited cause of the end-Permian crisis is the Siberian Traps large igneous province (LIP), which may have released large volumes of greenhouse gases and other harmful volatiles to the atmosphere during volcanism and through contact metamorphism (Black et al., 2012; 2014; Burgess and Bowring, 2015; Ernst and Youbi, 2017; Jones et al., 2016; Svensen et al., 2009; Figure 1). The end-Permian extinction is marked by a sharp negative carbon isotope ($\delta^{13}C$) excursion (Baud et al., 1989; Magaritz et al., 1988; Shen et al., 2012), indicating an environmental disturbance that involved the potential release of ^{12}C-rich carbon to the ocean-atmosphere system (Figure 2). The end-Permian extinction was followed by a 5 Myr period of lingering recovery of the benthos (Hautmann, 2014; Hautmann et al. 2015) and of explosive recoveries interrupted by massive extinctions of the nekton (Brayard et al., 2009; Brayard and Bucher, 2015; Orchard, 2007). These diverging biodiversity patterns were accompanied by large positive and negative $\delta^{13}C$ fluctuations (Payne et al., 2004; Meyer et al., 2011; Grasby et al., 2016; Song et al., 2013), including at the Smithian/Spathian boundary (SSB) in the middle of the Early Triassic (Galfetti et al., 2007b).

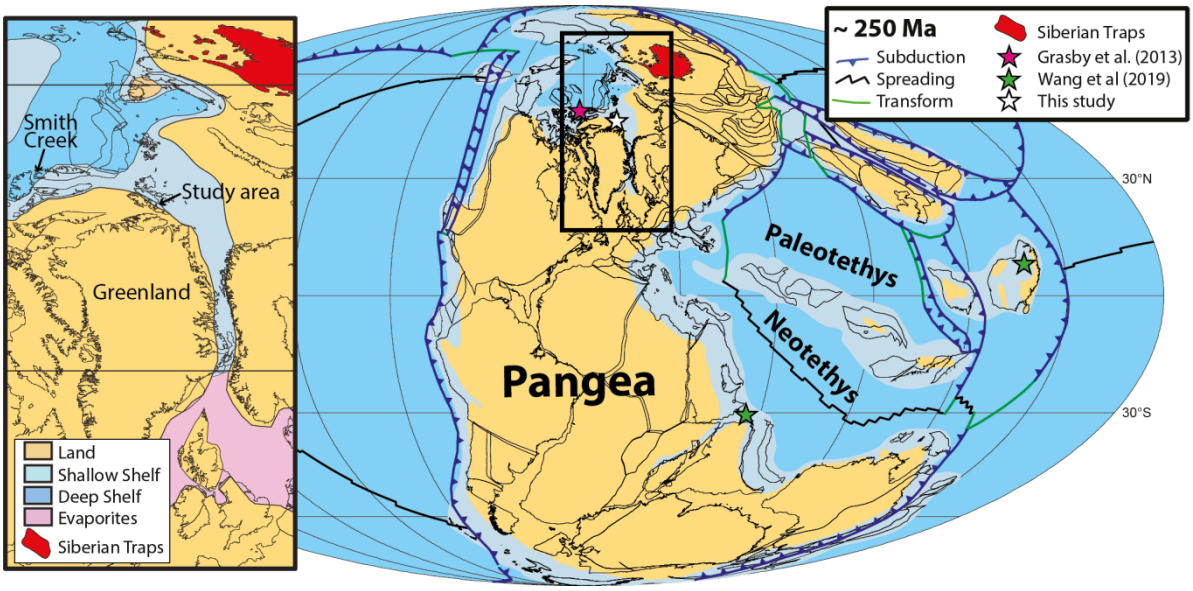

69

70 Figure 1. A paleogeographical reconstruction at around 250 Ma (Early Triassic), after Torsvik and Cocks (2017).
71 Postulated plate boundaries are marked, with solid blue lines denoting subduction zones with teeth on the
72 upper plate, black lines are spreading centres, and green lines are transform plate margins. Outlines of major
73 crustal units are shown in black. Predicted paleoshorelines are from Golonka (2011). The known extent of the
74 Siberian Traps LIP is shown in red. The pink star shows the sample locality used by Grasby et al. (2013), also the
75 type locality of the Smithian substage at Smith Creek, Ellesmere Island. The green stars show the sample
76 locations of Wang et al. (2019), while the white star shows the locality used in this study (see Figure 3).

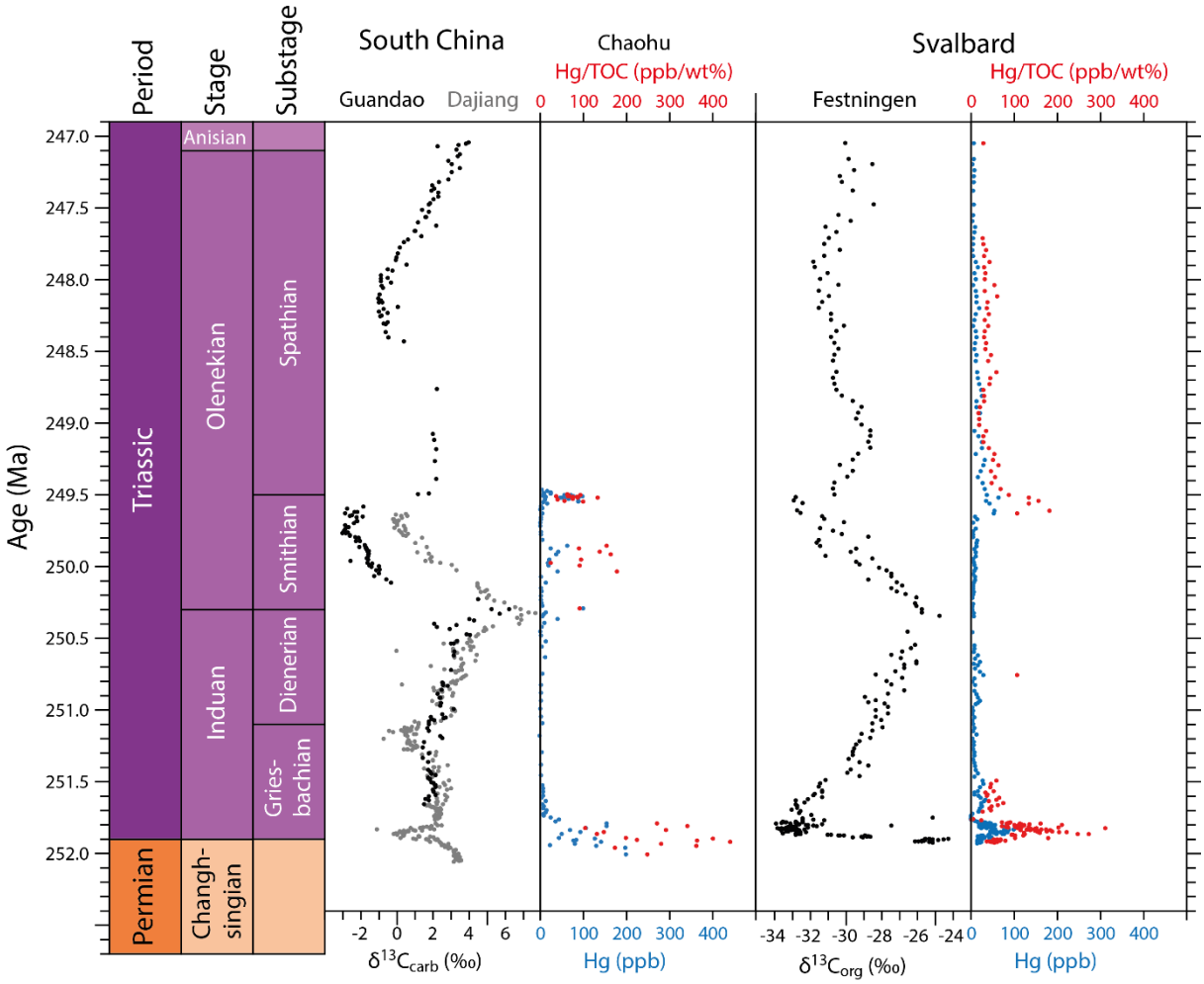

Figure 2. A summary of carbon isotope excursions and Hg anomalies in the Early Triassic. The South China $\delta^{13}C_{carb}$ data is from Meyer et al. (2011) and Payne et al. (2004), with the Guandao data points shown in black and the Dajiang data points shown in grey. Hg (blue) and Hg/TOC data from Chaohu are also shown (Wang et al., 2019). The Festningen $\delta^{13}C_{org}$, Hg (blue), and Hg/TOC (red) data from Svalbard are from Grasby et al. (2013; 2016). Hg/TOC values only shown where TOC >0.2 wt.% (Grasby et al. 2016), as TOC concentrations below this threshold result in errors in Hg/TOC values larger than any potential anomalies. These datasets have been calibrated with the latest generation of radio-isotopic ages (Burgess et al., 2014; Ovtcharova et al., 2015; Baresel et al., 2017). Constant sedimentation rates are assumed within each substage. Equal durations of the Griesbachian, Dienerian and Smithian substages are arbitrary because of the lack of radio-isotopic age dates. The duration of the Spathian is derived from the older generation of U-Pb ages (Galfetti et al., 2007b).

89 The Smithian was a period of intense carbon cycle instability, with a prolonged (100's kyr) and
90 significant (4-10 ‰) negative $\delta^{13}C$ excursion (Figure 2; Payne et al., 2004; Tong et al., 2007). In
91 contrast, the SSB is marked by a sharp positive $\delta^{13}C$ excursion (Payne et al., 2004) and a drastic
92 extinction of marine nektonic organisms (Orchard, 2007; Brayard and Bucher, 2015). Wang et al.
93 (2019) placed the SSB well after the onset of the CIE in South China, based on the first occurrence of
94 the conodont index *Novispathodus pingdingshanensis*. However, the first occurrence of this species
95 appears to be globally diachronous (Zhang et al., 2019), as it has been shown to co-occur with late
96 Smithian taxa as well (e.g., *Xenoceltites*, Komatsu et al., 2016; Goudemand et al., 2012; Orchard &
97 Zonneveld, 2009; *Glyptophiceras*, Romano et al., 2013; *Scythogondolella milleri*, Leu et al., 2018). The
98 late Smithian extinction unfolded in a stepwise pattern, with a first diversity decrease of ammonoids
99 during the early late Smithian *Wasatchites tardus* Zone (Brühwiler et al., 2010). It was followed by a
100 further decrease during the late late Smithian *Glyptophiceras sinuatum* Zone (Brühwiler et al., 2010),
101 where diversity was at its lowest (Brayard and Bucher, 2015), even lower than in the Permian-Triassic
102 boundary bottleneck (Brayard et al., 2009). At least in the low paleolatitudes, ammonoids
103 experienced an explosive re-diversification during the early Spathian (Brayard et al., 2006). The
104 diversity of conodonts followed a roughly parallel trend (Orchard, 2007) and this clade experienced
105 its last major evolutionary radiation from the SSB onward. Ecological communities of terrestrial
106 plants were most profoundly affected during the middle Smithian as manifested by the presence of a
107 spore spike (Hermann et al., 2011). Floras indicate a relatively more humid climate before the early
108 late Smithian *W.tardus* Zone compared to drier climatic conditions during and after the same zone,
109 but their ecological recovery was already well under way from the middle-late Smithian boundary on
110 (Hermann et al., 2011; Hochuli et al., 2016). The composition of marine vertebrate apex predators
111 was also reshuffled during the end-Smithian extinction, with the replacement of amphibians by
112 reptiles (Scheyer et al., 2014).

113 Zhang et al. (2019) provided a thorough review of the available definition(s) of the SSB by means of
114 ammonoids, conodonts, and carbon isotopes. In terms of ammonoids, these authors tacitly endorsed

115 the discrete and “natural” approach of biochronological boundaries as advocated by Lucas (2018),
116 which was and still is successfully employed and refined in Early and Middle Triassic ammonoid
117 biochronology. For the low latitudes, the current understanding in terms of ammonoids is that the
118 SSB is within the interval of separation bounded by the *Glyptophyceras-Xenoceltites* zone below
119 (Brühwiler et al., 2010) and the tirolitid n. gen. A beds above (Galfetti et al., 2007b). By no means
120 does this definition exclude the future intercalation of one or several additional zones within this
121 interval of separation. This can be anticipated from sections where the SSB global regression was
122 outstripped by local tectonic subsidence (Bucher, ongoing work). However, this definition is not
123 directly transferable to the high latitude record because: 1) correlatives of the late Smithian
124 *Glyptophyceras-Xenoceltites* zone are always absent in the boreal record where it has been removed
125 by the earlier onset of the SSB gap, and 2) the explosive diversification of tirolitids is restricted to low
126 latitudes. Our recent finding of the oldest tirolitid (= tirolitid n. gen. A in Galfetti et al. 2007b)
127 associated with *Bajarunia euomphala* in Nevada (Bucher, ongoing work) combined with the here
128 newly reported occurrence of *B. euomphala* 0.60 m above the base of the Vendomdalen Member at
129 Stensiöfjellet considerably narrows down the interval of separation containing the SSB in the
130 Spitsbergen record. There, the SSB is now bracketed by the top of the *Wasatchites tardus* Zone
131 below and the new base of the *Bajarunia euomphala* Zone above.

132 In terms of conodont Unitary Association zones, ongoing work by Leu et al. in several low latitude
133 records leads to improved accuracy and precision, but this is not directly relevant to the Spitsbergen
134 data presented here which rely on ammonoid age control.

135 Last but not least, the utilization of the carbon isotope record as a surrogate in the absence of age-
136 diagnostic fossils is directly dependent on the completeness of the record and sedimentation rates.
137 Considering the evidence for a global regression straddling the paleontologically defined SSB, great
138 care is needed when attempting detailed chemostratigraphic correlations during the late Smithian
139 and basal Spathian. We also presently document that the onset of the positive CIE is still within the

middle Smithian in Spitsbergen, thus newly highlighting an earlier inception of the CIE in the high latitudes. We additionally confirm that in Spitsbergen, the positive maximum of the CIE is within the basal Spathian.

Several studies have suggested the occurrence of late-phase volcanic activity of the Siberian Traps around the time of the SSB as a cause for "lethally" hot climate (e.g. Paton et al., 2010; Orchard 2007; Xie et al., 2010; Sun et al., 2012; Shen et al., 2019a). However, these studies rest on age controls that have been cast into doubt by recent literature, especially the hypothesis that the first occurrence of the conodont index *Novispathodus pingdingshanensis* is a synchronous marker defining the base of the Spathian (Goudemand et al., 2013; Zhang et al., 2019). Some other studies with correct age control also suggested that acidification through volcanogenic volatiles may have contributed to the late Smithian extinction (Galfetti et al. 2007). At present, the available radiometric ages of the Siberian Traps basalts are confined to close to the Permian-Triassic boundary (Burgess et al., 2014; Kamo et al., 2003). This may be a sampling bias due to the focus on this key horizon as over 1000 m of Early Triassic flows post-date this sequence (Kamo et al., 2003). Therefore, while there is evidence of continued Siberian Traps volcanism after the Permian-Triassic boundary, there are currently no time constraints on these eruptions and no direct evidence of elevated volcanic activity around the SSB.

One method used as a proxy for major volcanism in sedimentary sequences that has received considerable recent attention is the use of mercury (Hg) anomalies (Sanei et al., 2012). Mercury deposition is primarily driven by complexation with organic matter, such that a strong positive correlation exists between Hg and total organic carbon (TOC) in many sedimentary sequences (Outridge et al., 2007; Ruiz and Tomiyasu, 2015; Sanei et al., 2014). It is assumed that positive anomalies of Hg/TOC values occur when elevated Hg emissions are released into the environment, resulting in alternate modes of Hg deposition to organic matter drawdown, such as in sulfides or adhered to clays (Sanei et al., 2012; Shen et al., 2019b). Volcanic activity is one of the primary

atmospheric Hg sources in the present time (Pyle and Mather, 2003). Therefore, sharp increases in Hg/TOC values preserved in the sedimentary record have been traditionally interpreted as a proxy for enhanced volcanism. Hg/TOC anomalies have been reported from several of the major environmental crises, including the end-Permian (Sanei et al., 2012; Grasby et al., 2013; 2016), end-Triassic (Thibodeau et al., 2016; Percival et al., 2017), Cretaceous-Paleogene (Sial et al., 2013; Font et al., 2016; Keller et al., 2018) and the Paleocene-Eocene (Keller et al., 2018; Jones et al., 2019).

However, several recent studies have suggested Hg/TOC anomalies can be caused by non-volcanic factors. Clay mineral surfaces and sulfides can also host Hg (Ravichandran, 2004; Selin, 2009), so conditions that favour Hg-uptake into these fractions may be important. Measurements across Jurassic and Cretaceous Oceanic Anoxic Events (Percival et al., 2018; Them II et al., 2019) suggest that Hg/TOC anomalies correlate with proximity to paleoshoreline, potentially indicative of clay-hosted Hg (Them II et al., 2019). The redox properties of depositional waters are also a key factor, as reducing conditions favour the formation of HgS and incorporation of Hg into iron sulfides (Bower et al. 2008, Duan et al., 2016). Euxinic conditions appear to favour sulfide-hosted Hg over organic-hosted Hg, which can create the appearance of Hg/TOC anomalies in pyrite-dominated successions such as in Ordovician/Silurian boundary sections (Shen et al., 2019b). Finally, changes to organic matter sourcing can result in apparent Hg/TOC 'anomalies', due to variations in Hg-uptake into organic matter in numerous marine and terrestrial ecosystems (Percival et al., 2018; Jones et al., 2019). It is therefore of great importance to investigate multiple sections across a specific time interval to gain a true understanding of the origins of any Hg/TOC anomalies in marine sediments (Them II et al., 2019; Jones et al., 2019).

In the case of the SSB marine extinction and associated ecological turnover of floras, a detailed stratigraphic relationship between Hg/TOC anomalies, anoxia, organic matter, and the distribution of global stratigraphic gaps is required to fully assess the possibility of volcanism as a primary trigger of the environmental disturbances. Several studies have published Hg/TOC variations through the Early

Triassic (Figure 2). Grasby et al. (2013) measured Hg/TOC values at Smith Creek, Sverdrup Basin, Arctic Canada (Figure 1), which is the type section of the Smithian substage (Tozer, 1967). Modest Hg/TOC anomalies are recorded from the middle Smithian (Figure 2), which overlap with the onset of the large negative $\delta^{13}C$ excursion (ca. 470 to 550 m). Background Hg/TOC values are observed in the early late Smithian and across the SSB, with a brief return to modest Hg/TOC anomalies in the early Spathian (ca. 590 to 610 m; Fig. 3 in Grasby et al., 2013). At Smith Creek (Tozer, 1967), late Smithian ammonoids occur in a somewhat condensed carbonate horizon near 570 m and are exclusively assigned to the early late Smithian *Wasatchites tardus* Zone. Together with the very abrupt lower flank of the positive carbon isotope excursion, it strongly suggests the presence of a hiatus straddling the latest Smithian (*Glyptophiceras sinuatus* Zone of Brühwiler et al., 2010). Subsequently, Grasby et al. (2016) described extensive geochemical records from the Permian Kapp Starostin Formation up to the Spathian Tvillingodden Formation at Festningen, western Spitsbergen. This locality represents a near-shore, shallow water setting (Mørk et al., 1982; Wignall et al., 2016) that lacks adequate biostratigraphic control. There are pronounced Hg/TOC anomalies that begin close to the peak of the late Smithian negative $\delta^{13}C$ excursion and continue to the peak of the positive $\delta^{13}C$ excursion of the early Spathian (Figure 2). These results and interpretations stand in marked contrast with the Tethyan SSB records from Guryul (Kashmir) and Chaohu (South China), which do not reveal any clear Hg/TOC anomaly concomittent with the late Smithian positive CIE (Wang et al., 2019). However, a limiting factor with both of these data sets (Grasby et al., 2016; Wang et al., 2019) is that TOC concentrations for much of the Early Triassic are extremely low in these sections (Figure 2). The recommended limit for interpreting Hg/TOC concentrations is 0.2 wt% (Grasby et al., 2016), with errors below this arbitrary threshold considered greater than potential Hg/TOC anomalies. While the latest Smithian Hg/TOC values appear to be anomalously high compared to early Spathian strata (Figure 2; Grasby et al., 2016; Wang et al., 2019), it is not possible to assess whether these elevated latest Smithian Hg/TOC values are an isolated event. It is possible that similar Hg/TOC values are present in mid Smithian sections with higher TOC concentrations.

Here, we report on the mercury record, organic carbon isotope, and trace element data across the Smithian-Spathian boundary at Wallenbergfjellet in central Spitsbergen. This represents a more distal (offshore) depositional setting to the Festningen section (Grasby et al., 2016), with adequate biostratigraphic age control.

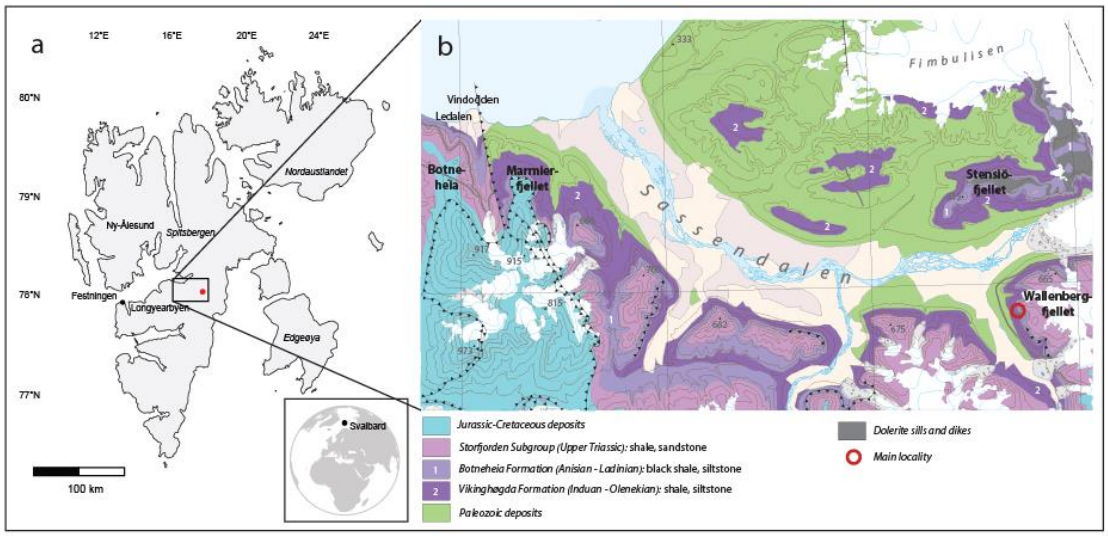

Figure 3. Map of Svalbard with the studied locality at Wallenbergfjellet, Spitsbergen. a) The location of the study area and the Festningen site used by Grasby et al. (2016). b) Geology of the study area, lithologies are redrawn from geological maps of Svalbard (Major et al., 2001).

2. Geological setting and age controls

A geological map of the study area is shown in Figure 3. In central Spitsbergen the Lower Triassic succession is stratigraphically defined as the Vikinghøgda Formation, which represents an offshore (> 50 km from shore, e.g. Wignall et al. 2016) shelf environment that is the distal continuation of the coastal and shallow marine deposits of the time equivalent Vardebukta and Tvillingodden formations of western Spitsbergen (Festningen section). The lower member of the Vikinghøgda Formation, the Deltadalen Member, is Griesbachian to Dienerian in age and equivalent to the Vardebukta Formation. The Lusitaniadalen and Vendomdalen members roughly represent the Smithian and Spathian

substages and are time equivalent to the Tvillingodden Formation (Mørk et al., 1999; Wignall et al., 2016). The Vikinghøgda Formation is a deposit of sandy silts grading into silty grey shales and silty black shales. Horizons of calcareous nodules and calcareous paper shale are widespread in the Lusitaniadalen and Vendomdalen members. The formation was deposited on a gently sloping marine ramp during stepwise deepening (Mørk et al. 1999; Wignall et al. 2016). The stratigraphic boundary between the Lusitaniadalen Member and the Vendomdalen Member is defined as the top of a yellow-weathering cemented sandstone (Mørk et al., 1999). The level roughly corresponds to a shift from grey shale to dark grey paper shale, which is often apparent in the field. At Wallenbergfjellet, the shift to dark grey paper shale was in some places found to overlie the defined boundary with a few tens of centimeters.

Brühwiler et al. (2010) first established that the latest Smithian *Glyptophiceras sinuatum* Zone overlies the early late Smithian *Wasatchites distractus* Zone in recently studied Tethyan sections from the northern Indian margin. The same succession has been subsequently confirmed in several sections of the western USA basin (Jattiot et al., 2017; Jenks and Brayard, 2018). The *W. distractus* Zone and the *G. sinuatum* Zone correlate with the lower and the upper parts of the more comprehensive *Anasibirites multiformis* beds as initially described by Brayard and Bucher (2008) in the Nanpanjiang Basin. The *A. multiformis* Zone of these authors was synonymous with the entire late Smithian record preserved in South China, but ongoing work indicates that in fact, the *W. distractus* and the *G. sinuatum* zones consistently occur in superposition within the late Smithian black shales of the Nanpanjiang Basin, in perfect agreement with other sections from the northern Indian margin and the western USA. Therefore, the scope of the low paleolatitude *A. multiformis* Zone must be reduced to the first zone of the late Smithian (Jattiot et al., 2015). The *A. multiformis* Zone is a strict correlative of the *W. distractus* Zone in the high latitudes. Hence, the low paleolatitude records show that the *G. sinuatum* Zone systematically occurs within the upper half of the late Smithian positive CIE, immediately preceding the heaviest values and the abrupt return to lighter values in the early Spathian. The boundary between the Smithian and Spathian substages in

259 the Boreal Realm was defined by the last occurrence of the ammonoid *Wasatchites tardus*, which is
260 the oldest of the two late Smithian ammonoid zones (Brühwiler et al., 2010). This definition avoids
261 the fact that the paleontological boundary between the Smithian and the Spathian is within a longer
262 gap whose base includes the *G. sinuatum* Zone in the Sverdrup Basin, in northern Siberia, in NE
263 British Columbia and in Spitsbergen. The onset of the global late Smithian gap is thus earlier in the
264 Boreal record than within the Tropics.

265 A widely used proxy for the Smithian/Spathian biostratigraphic boundary is the presence of a global
266 positive $\delta^{13}C$ excursion. In Dicksonland, central Spitsbergen, Galfetti et al. (2007a) first established
267 that the end of the positive CIE is within the lower part of the Vendomdalen Member. At variance
268 with their earlier paper on the Sverdrup Basin (Grasby et al., 2013), Grasby et al. (2016) placed the
269 SSB at Festningen, western Spitsbergen, at the minimum of the $\delta^{13}C$ curve, i.e. at the base of the
270 onset of the positive $\delta^{13}C$ excursion, and in coincidence with the Hg/TOC anomalies. However, this
271 placement of the boundary with respect to the CIE at Festningen (Grasby et al., 2016) is in conflict
272 with other data. In the Tethyan ammonoid and carbon isotope records (Brühwiler et al., 2010;
273 Galfetti et al., 2007b), the substage boundary is rather associated with the end of the ascending limb
274 of the positive CIE. Even if the *G. sinuatum* Zone corresponds to a gap in the Boreal record, the
275 isotope records from Dicksonland (Galfetti et al., 2007a) demonstrate that the maximum of the
276 positive CIE is within the lower part of the Vendomdalen Member, which is of early Spathian age, and
277 that it has a gently gradual shape, not a spike shape like in most low latitude records. At
278 Wallenbergfjellet, the end of this positive CIE is also found in the lower part of the Vendomdalen
279 Member, whose age is not well constrained in terms of ammonoids. However, at Stensiöfjellet (only
280 5 km north of Wallenbergfjellet) where the stratigraphic sequence is similar, we found a basal
281 Spathian ammonoid fauna characterized by *Bajarunia euomphala* 60 cm above the base of the
282 Vendomdalen Member, i.e. within the maximum of the positive CIE.

Thick sills of Early Cretaceous age (the Diabasodden Suite) were emplaced into the Triassic succession throughout central Spitsbergen. At Wallenbergfjellet, a large intrusion, locally expressed as a 10 m thick dyke, crops out a few hundred meters away from the studied section. It is possible that this dyke is connected to a sill underlying the section of similar thickness to the dyke. Based on the uninterrupted stratigraphic succession for at least 100 m below our studied interval we assume that such a sill has not disturbed the geochemistry to any serious degree. In the Upper Triassic at Botneheia in Central Spitsbergen, Hubred (2006) reported little thermal effect on organic matter outside an aureole of ca. 1.5 times the sill thickness.

3. Material and methods

3.1. Sampling

In 2017 we collected 48 shale samples from the Wallenbergfjellet section, from 18 m below the base of the Vendomdalen Member to the base of the overlying Botneheia Formation (Anisian). The section was sampled at 2 m intervals, with the exception of the interval from 6 m below to 4 m above the base of the Vendomdalen Member, which was sampled at 1 m intervals (Figure 4). We collected ammonoids from throughout the section, although the lower part of the Vendomdalen Member yielded only few and poorly preserved specimens. Some ammonoids reported in Figure 4 were found in adjacent sections with the same lithological development.

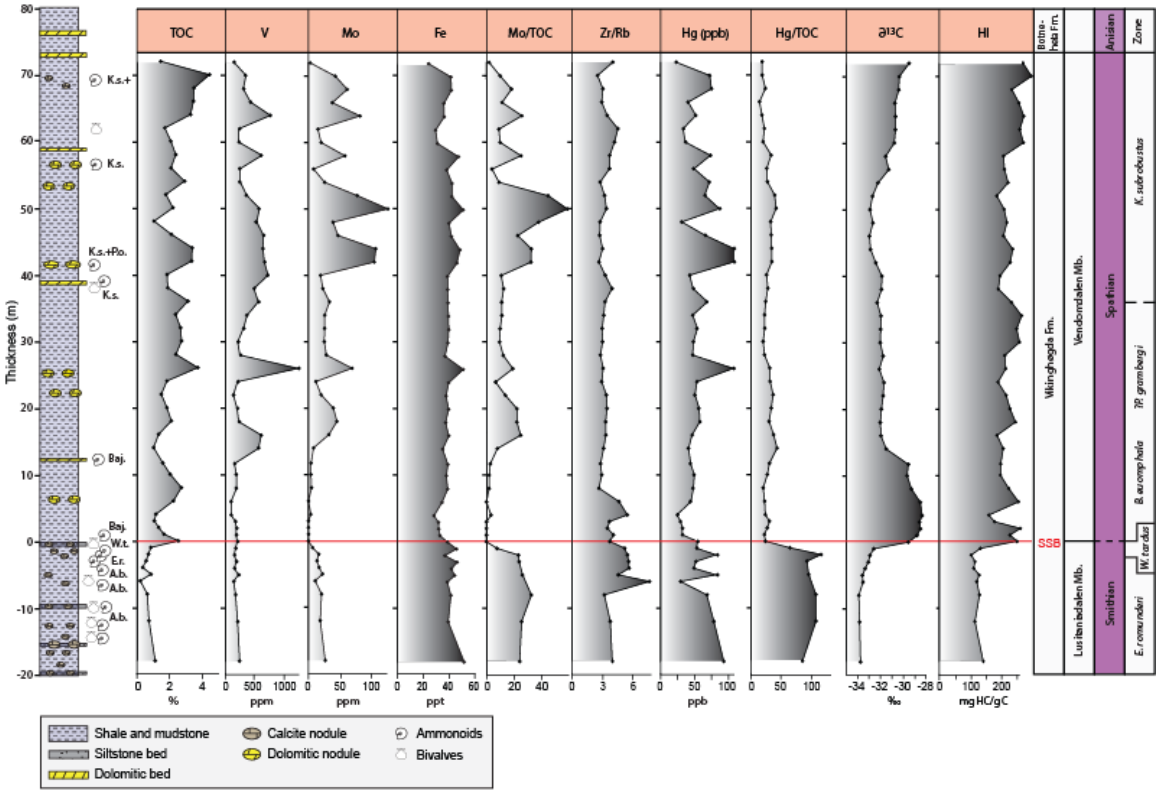

Figure 4. Lithological log, biostratigraphy and geochemical logs from the Wallenbergfjellet section. Two samples (-6 and -4 m) had TOC < 0.5 %, and Mo/TOC and Hg/TOC were therefore discarded (Them II et al., 2019). Some ammonoids in the Vendomdalen Member were found in adjacent sections. Ammonoids listed are A. b.: *Arctoceras blomstrandi*; E. r.: *Euflemingites romunderi*; W. t: *Wasatchites tardus*/*Xenoceltites* spp./*Anasibirites kingianus* assemblage; Baj.: *Bajarunia* sp.; K. s.: *Keyserlingites subrobustus*; P. o.: *Popovites occidentalis*; K. s.+: *K. subrobustus*/*Svalbardiceras spitzbergensis*/*S. freboldi*?/*P. occidentalis*/*Pseudosageras* sp./*Procarnites* sp. assemblage.

3.2. Mercury analysis

Mercury analysis was conducted at the University of Oxford using the Lumex RA-915 Portable Mercury Analyser with a PYRO-915 pyrolyzer (Bin et al., 2001). Analytical procedures followed in-

316 house protocols (Percival et al., 2017; Jones et al., 2019), where between 40-60 mg of powdered
317 sample was weighed before being transferred to the pyrolyzer and heated to 700 °C. Sample peaks in
318 the spectrometer were calibrated using the NIMT/UOE/FM/001 peat standard with a known Hg
319 concentration of 169 ±7 ppb, with repeat calibrations every ten samples to negate any drift in the
320 instrument. Each sample was run in duplicate, which resulted in an analytical error of ±5 %.

321 *3.3. Handheld XRF and SEM-EDX*

322 Flat pieces were selected from each sediment sample, washed and analysed using handheld X-ray
323 fluorescence spectroscopy (HHXRF). The instrument used was a Thermo Scientific Niton XL3t
324 GOLDD+ with an aperture of 8 mm. Integration time was 120 s in the "Mining Cu/Zn" mode. After
325 every five samples, a calibration measurement was taken on a pressed powder pellet of the USGS
326 Columbia River Basalt BCR-2 standard, diluted to four parts powder and one part binder. The diluted
327 standard has a certified V concentration of 416 ± 14 (1 σ) ppm. No drift in the V measurement of the
328 standard was observed, and the variance was relatively small, with average V concentration 420 ± 24
329 (1 σ) ppm, N = 10, i.e. within the error of the certified standard value. Using the same instrument
330 model, Schovsbo et al. (2018) reported excellent correlation between HHXRF and ICP-MS values for V
331 and Mo in dark shales (R^2 = 0.98 and R^2 = 0.96, respectively) over wide ranges. Still, we regard the V,
332 Mo, Fe and Zr/Rb curves obtained as semi-quantitative.

333 SEM and EDX microimaging was carried out on selected samples to investigate distributions of iron
334 and pyrite, using a Hitachi S-3600N SEM in the backscatter (BSE) mode and with a Bruker XFlash 5030
335 energy dispersive X-ray detector (EDX), at the Natural History Museum in Oslo.

336 *3.4. Organic geochemistry*

337 Total organic carbon content (TOC) was measured by Applied Petroleum Technology, Oslo, Norway,
338 with a Leco SC-632 instrument. Diluted HCl was added to the powdered sample to remove carbonate.
339 The sample was then introduced into the combustion oven, and the amount of carbon was measured

as carbon dioxide by an IR-detector. Rock-Eval pyrolysis used the Rock-Eval 6 instrument at 300 °C for 3 min, increasing by 25 °C/min to 650 °C. The Jet-Rock 1 standard was run as every tenth sample and checked against the acceptable ranges according to the Norwegian Industry Guide to Organic Geochemical Analysis (NIGOGA), 4th edition.The permissible range for TOC in the Jet-Rock standard is 11.3-12.5 %.

3.5. Bulk organic carbon isotope analysis

Carbon isotope analysis was carried out at Liverpool University. Approximately 0.5 g of powdered sample was weighed into a glass beaker and carbonate minerals (and other acid soluble phases) were removed by reaction with 40 ml of 1M HCl (pH 0.0) at 35 ^{o}C for 24 h. Following decomposition the acid insoluble residue was recovered by centrifugation, washed free of any remaining acid by repeated cycles of rinsing with deionised water, and freeze-dried.

Carbon dioxide for mass spectrometric measurement of carbon ($^{13}C/^{12}C$) isotope ratios in samples of organic carbon was prepared using a modification of the classical 'sealed tube' combustion procedure described by Frazer and Crawford (1963) and Sofer (1980). Decarbonated (1M HCl, 35 ^{o}C, 24 h) bulk sediment samples (sufficient to yield ~100 μmols of CO_2) were weighed into silver foil capsules and loaded into pre-conditioned (650 ^{o}C, 24 hrs) quartz tubes together with 3 g of Cu(II)O and 0.5g of Cu metal. All tubes were then sealed under vacuum and organic carbon was converted to CO_2 by combustion at 850 ^{o}C for 2 hrs. Following combustion the tubes were allowed to cool to 600 ^{o}C (and held for 4 hrs) in order to allow conversion of any nitrous oxide (in contact with Cu metal) to nitrogen before final cooling (~16 hrs) to room temperature.

Product CO_2 was recovered under vacuum using standard cryogenic separation procedures (to remove H_2O and N_2) and the amounts of the component masses (*m/z* 44, *m/z* 45, *m/z* 46) were measured with respect to a comparison (reference) CO_2 using a VG SIRA 10 dual-inlet, gas source

mass spectrometer. Resultant delta values ($\delta_{CO_2}^{45/44}$ and $\delta_{CO_2}^{46/44}$) were subsequently corrected for ^{17}O contributions (Craig, 1957), and calibrated to the Vienna Pee Dee Belemnite (VPDB) carbon isotope scale *via* measurement of CO_2 prepared from multiple aliquots of an in-house Carrara marble (LIVM2) calcite ($10^3\delta^{13}C_{VPDB}$= +1.98) and a polyethylene (IAEA-CH7) international reference material ($10^3\delta^{13}C_{VPDB}$= -32.15) run with each batch of unknowns. Isotopic ratios are reported as conventional delta values with respect to the VPDB scale ($\delta_{OC}{}^{13}C_{VPDB}$)

All sample data were normalized against LIVM2-CH7 such that $\Delta_{LIVM2\text{-}CH7}$= 34.13‰. Analytical precision (2σ) is estimated to be better than ±0.1 ‰ based on the replicate measurement of IAEA-CH7.

Data were plotted and analyzed with the software Past, v. 3.18 (Hammer et al., 2001).

4. Results

4.1. Ammonoid biostratigraphy

The lithological log, biostratigraphy and geochemistry are shown in Figure 4. Ammonoids were collected from carbonate nodules and lenticular horizons throughout the section. Ammonoids identified at -4.3 m and below in the section are mostly *Arctoceras* cf. *blomstrandi* and *Juvenites spathi* belonging to the comprehensive *E. romunderi* Zone of middle Smithian age. *Euflemingites* itself was found at -3.0 m, and *Juvenites spathi* at -2.0 m. At -1.3 m, -1.2 m and immediately below the base of the Vendomdalen Member, an abundant ammonoid fauna from the *W. tardus* Zone (early late Smithian) was recovered, with *Wasatchites tardus*, *Xenoceltites* spp., *Arctoprionites* sp. and *Anasibirites kingianus*. The *W. tardus* Zone is therefore recognized from ca. -2.0 m to the top of the Lusitaniadalen Member.

Ammonoids are more scattered and generally poorly preserved in the Vendomdalen Member. A *Bajarunia* sp. indet. at 12 m is indicative of the *B. euomphala* Zone, early Spathian. *Keyserlingites subrobustus* was found from 39 m almost to the top of the Vendomdalen Member, documenting a thick late Spathian *K. subrobustus* Zone. An interval with small, gray carbonate nodules near the top of the member contains a rich, well-preserved late Spathiancephalopod fauna (cf. Mørk et al., 1999) with *K. subrobustus*, *Svalbardiceras spitzbergensis*, *S. freboldi*?, *Popovites occidentalis*, *Pseudosageras* sp., *Procarnites* sp. and orthocone nautiloids.

4.2. Carbon and trace element geochemistry

TOC values are low (< 1.2 wt.%) in the Lusitaniadalen Member (Figure 4). In the Vendomdalen Member the TOC is variable but higher, averaging 2.3 wt.% and reaching 4.4 wt.% in the upper part. Vanadium content is below 270 ppm in the Lusitaniadalen Member and the lower 12 m of the Vendomdalen Member. The upper part of the Vendomdalen Member has variable but higher V content, with an average of 450 ppm. Molybdenum shows a similar pattern as V, with values below 30 ppm up to 12 m, then increasing to an average of 44 ppm in the upper part. Average 2σ precision (repeatability) on V across all samples is 48 ppm, on Mo 2.6 ppm.

Zr/Rb values are generally below 4 in most of the section, but with elevated values (up to ca. 7) from -6 to +6 m. As zirconium is more prevalent in coarser, lithic grains and rubidium binds preferentially to clay particles, the Zr/Rb can be used as a proxy for grain size (Dypvik and Harris, 2001). The higher Zr/Rb values around the Lusitaniadalen-Vendomdalen member boundary therefore indicate coarser grain size, compatible with a more proximal depositional setting.

The vanadium values throughout the Wallenbergfjellet section are much higher than the 50 ppm reported from the Early Triassic of Western Spitsbergen by Wignall et al. (2016), but this difference is probably due to higher aluminium content in the more distal, finer-grained facies at this locality. Vanadium is a redox sensitive element (e.g., Tribovillard et al, 2006), indicating relatively more oxygenated bottom water conditions in the -18 m to +12 m interval than in the upper part of the

413 section. This is supported by low (< 1.5%) TOC values in the Lusitaniadalen Member, although TOC
414 increases to almost 3% already at the base of the Vendomdalen Member. V and TOC are positively
415 correlated through the section (R=0.48, p<0.001, N=48). Molybdenum shows the same pattern,
416 correlating strongly with V (R=0.65, p<0.001, N=48).

417 The Niton HHXRF is known to be imprecise for light elements, and Schovsbo et al. (2018) found very
418 poor correlation with ICP-MS data for Al. We do therefore not present curves for V/Al, Mo/Al or
419 Hg/Al. However, the lithology does not vary strongly through our section, and also the measured Al
420 values vary within only a small range (ca. 6 to 8 %). Normalization for Al would therefore probably
421 not change the general trends to any large degree.

422 Molybdenum is generally a redox sensitive element (Tribovillard et al., 2006), although only very high
423 Mo values (> 25 ppm) can be used to infer euxinic conditions, while lower values cannot be
424 interpreted unambiguously with respect to redox conditions (Hardisty et al., 2018).

425 The hydrogen index (HI) from the Rock-Eval analysis is consistently below 140 (~120 on average) in
426 the Lusitaniadalen Member, suddenly increasing to above 160 (~225 on average) in the
427 Vendomdalen Member (Figure 4). The oxygen index (not shown) shows the opposite pattern, with
428 high values (average 120) in the Lusitaniadalen Member decreasing to an average of 30 in the
429 Vendomdalen Member. The sudden increase in the hydrogen index at the base of the Vendomdalen
430 Member is in accordance with the results of Mørk et al. (1999), who noted a shift in type of organic
431 matter from type III kerogen (i.e. of more terrestrial origin) to mixed type II/III at the same
432 stratigraphic level. This was accompanied by a reduction in terrestrial palynodebris and a shift to
433 mainly marine plankton (Mørk et al., 1999). Our preliminary, high-resolution palynological
434 investigations from Wallenbergfjellet do not indicate a sudden, clear increase in marine organic
435 matter across the SSB that matches the rapid shift in Rock-Eval values. Another possible mechanism
436 for the increase in hydrogen index is decreased oxidation and/or decreased bioturbation (e.g.,
437 Durand and Monin, 1980) in the less oxic (higher TOC) facies of the Vendomdalen Member.

438 The organic $\delta^{13}C$ curve shows rather negative values in the Lusitaniadalen Member (between -33.84
439 and -32.55 ‰) with a slight positive trend in the upper part (Figure 4). An abrupt positive shift to -
440 29.53 ‰ at the base of the Vendomdalen Member marks the onset of a positive excursion in the
441 interval from 0 to 11.7 m. Isotope values remain fairly stable around -32 ‰ until about 40 m in the
442 section, followed by a slight negative excursion and a trend towards more positive values from ca. 50
443 m to the formation top. Interestingly, the gradual onset of the positive CIE starts in the middle
444 Smithian (Figure 4), which suggests a somewhat earlier inception than in the low paleolatitudes. The
445 smooth end of the positive CIE is 3-4 m above the base of the Vendomdalen Member, in agreement
446 with the record from Dicksonland, Spitsbergen (Galfetti et al., 2007a), although the coarser sampling
447 from Dicksonland does not allow restoring the gradual and smooth shape of the end of the excursion.
448

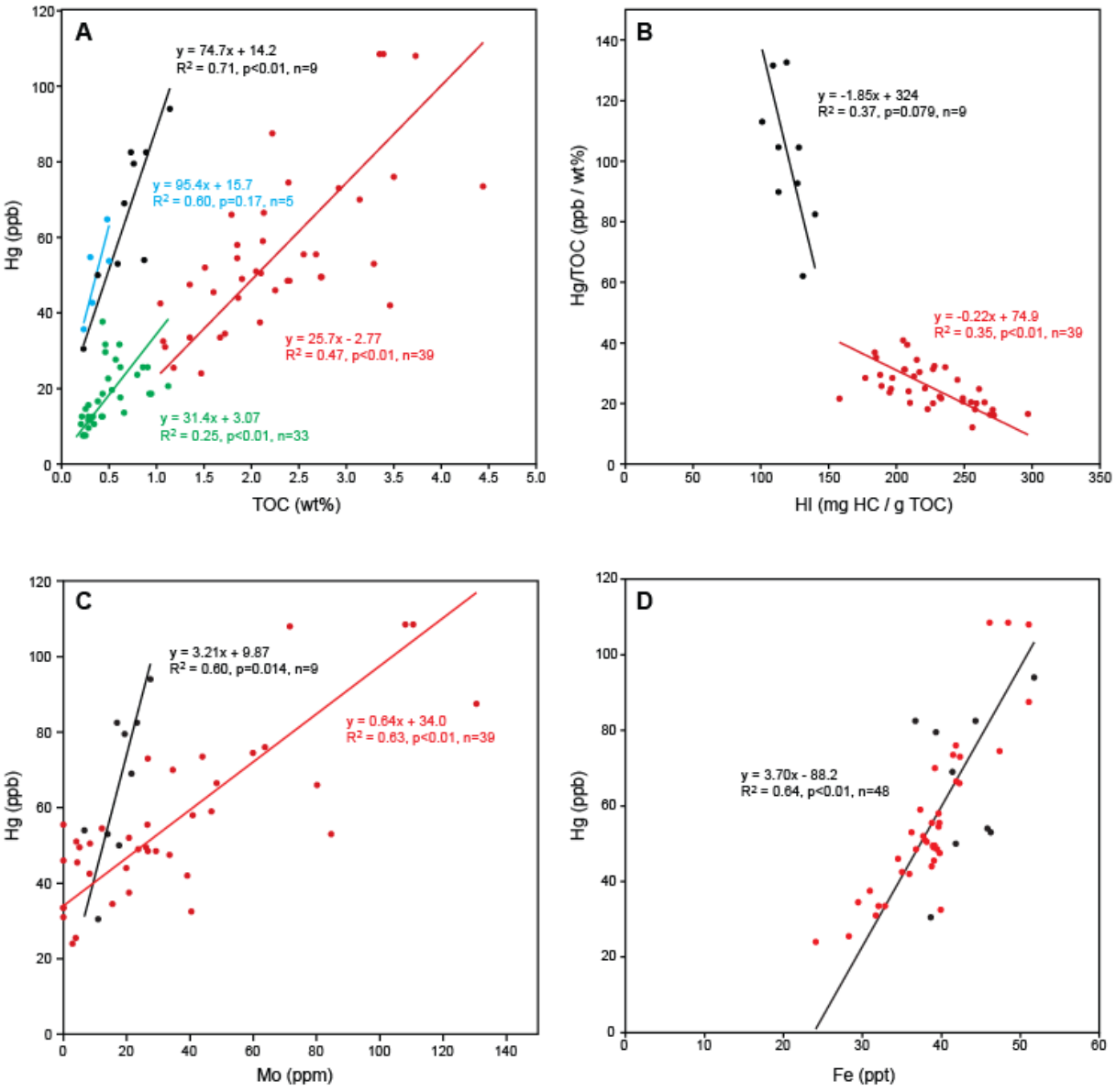

Figure 5. A: Cross plot of total organic content (TOC) versus Hg. Black: Smithian samples (below 0 m in the section; Lusitaniadalen Mb.) at Wallenbergfjellet, central Spitsbergen (this study). Red: Spathian samples (above 0 m; Vendomdalen Mb.) at Wallenbergfjellet. Blue: Smithian at Festningen, western Spitsbergen, data from Grasby et al. (2016). Green: Spathian at Festningen. Regression lines are based on the RMA method; *p* values computed by permutation test on R^2. Slopes are significantly different between the Smithian and Spathian (χ^2=11.7, p<0.01). Slopes are not significantly different between Wallenbergfjellet and Festningen. B: Hydrogen index (HI) versus Hg/TOC in the Smithian (black) and Spathian (red) at Wallenbergfjellet. C: Molybdenum (Mo) versus Hg in the Smithian (black) and the Spathian (red) at Wallenbergfjellet. D: Fe versus Hg in the Smithian (black) and Spathian (red) at Wallenbergfjellet.

459

460 *4.3. Mercury*

461 Mercury concentrations range from 24 to 109 ppb throughout the section. Although these values are
462 relatively low, they are generally about two times higher than the nearshore locality in western
463 Spitsbergen (Grasby et al., 2016). Mercury concentrations are highest in the Lusitaniadalen Member
464 and sporadic parts of the upper Vendomdalen Member (Figure 4). However, normalizing to TOC
465 shows a completely different picture with anomalously high Hg/TOC values (62–132 ppb/wt%) in all
466 Lusitaniadalen Member samples. In contrast, all Vendomdalen Member samples have low Hg/TOC
467 values (12–41 ppb/wt%). As shown in Figure 5A, there is strong correlation between TOC and Hg in
468 both Spitsbergen localities, but with considerably higher regression slope in the Lusitaniadalen
469 Member than in the Vendomdalen Member. The largest Hg/TOC values are documented in the
470 interval from -6 to -2 m in the section. The plateau-like Hg/TOC anomaly of the Lusitaniadalen
471 Member is present throughout the middle Smithian, as indicated by the ammonoid age control. The
472 Hg/TOC anomaly decreases within the early late Smithian and reached background values during the
473 early Spathian at the latest (Figure 4). The Hg/TOC and $\delta^{13}C$ curves appear discontinuous at this level,
474 supporting the presence of a hiatus in the uppermost Smithian (i.e. the missing *G. sinuatus* Zone).
475 The observation that the Hg/TOC anomaly largely precedes the positive CIE is in agreement with the
476 record obtained from a more proximal setting in West Spitsbergen as analysed by Grasby et al.
477 (2016). Therefore, this dataset suggests that a clear and sustained Hg/TOC anomaly was present in
478 the middle Smithian, which had disappeared by the early Spathian. TOC concentrations in the
479 Choahu section (Wang et al., 2019) are too low in the mid to late Smithian to allow meaningful
480 analyses of whether Hg/TOC anomalies are present (Figure 2).

481 Iron is present at 25-50 ‰ throughout the section (Figure 4). In the Smithian, SEM-EDX images
482 indicate that Fe is present both in euhedral pyrite and clastic mineral grains (Figures 6A, C). In the
483 Spathian, Fe is largely confined to euhedral and framboidal pyrite (Figures 6B, D).

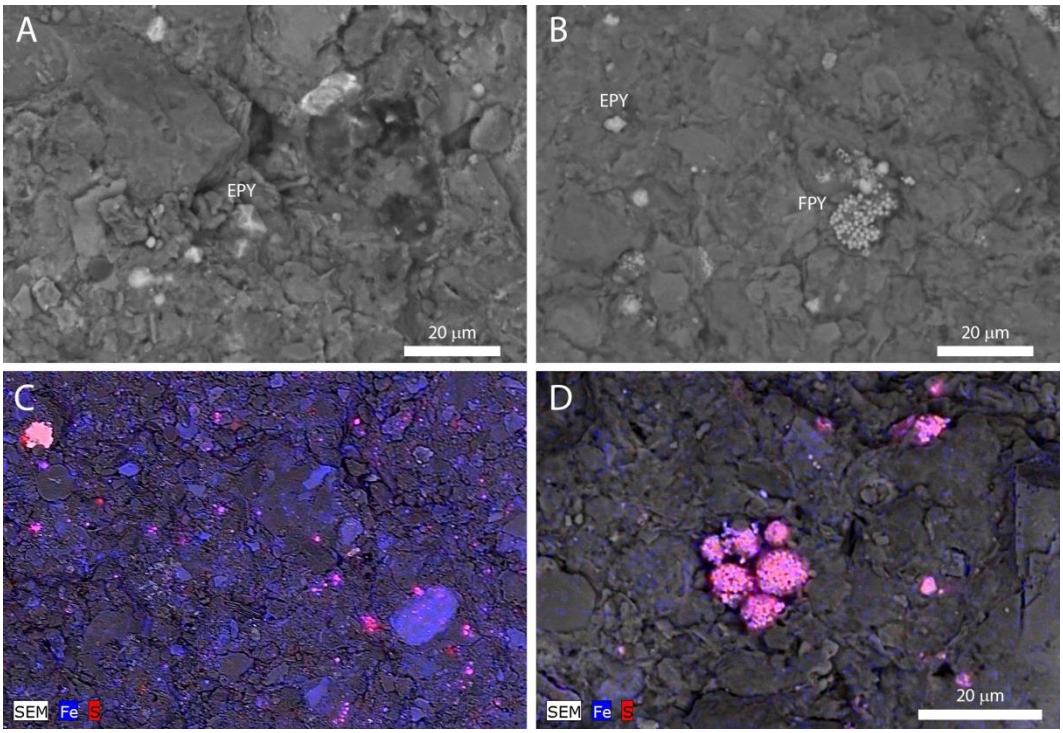

Figure 6. SEM-EDX images from the Wallenbergfjellet section: A: BSE image from -18 m in the section (Smithian). Note euhedral pyrite (EPY). B: BSE image from 60 m (Spathian). Note euhedral (EPY) and framboidal (FPY) pyrite. C: BSE and element map (EDX) image showing distribution of Fe (blue) and S (red) at -18 m (Smithian). Iron is found both in scattered euhedral pyrite grains and in other minerals. D: BSE and element map image from 60 m (Spathian), showing well-developed framboidal pyrite, with little Fe in the matrix.

5. Discussion

The comparison of the Wallenbergfjellet SSB section and the Festningen section of Grasby et al. (2016) strongly suggests the presence of a latest Smithian gap in Spitsbergen. This gap may be coeval with that of the Sverdrup Basin (Smith Creek; Grasby et al., 2013). In both basins, the latest Smithian *G. sinuatum* Zone is missing. In the well-studied ammonoid record from northern Siberia (Dagys, 1994) and NE British Columbia (Tozer, 1994), the only documented late Smithian zone is the *W. tardus* Zone, which consistently suggests an earlier onset of the gap on shelves in Siberia, the

499 Canadian Arctic, NE British Columbia and Spitsbergen. This timing contrasts with the majority of low
500 paleolatitude SSB sections where the *G. sinuatum* Zone is found above the *A. multiformis* Zone,
501 which is a strict correlative of the boreal *W. tardus* Zone. This diachronous worldwide gap, along with
502 the latest Smithian and earliest Spathian temperature and/or salinity changes (Romano et al., 2013;
503 Goudemand et al., 2019) and the earlier (middle-late Smithian boundary) switch from wet to dry
504 climate indicated by terrestrial plants (Hermann et al., 2011; Hochuli et al., 2016) are all pointing to a
505 transition from a greenhouse to a more temperate or even cold climate during the late Smithian,
506 with a modest extension into the basal Spathian. The middle Smithian recorded the most prominent
507 negative CIE of the Early Triassic, coeval with changes in temperature and/or salinity (Romano et al.,
508 2013), a major spore spike (Hermann et al., 2011) and Hg/TOC anomalies only known from the boreal
509 record (Grasby et al., 2013; 2016). The earlier onset of the gap in the Boreal realm also supports early
510 cooling at high latitude, thus choking the terrigenous flux towards marine shelves during the *G.*
511 *sinuatum* Zone. In an equatorial SSB section from the South China block, a multiproxy geochemical
512 analysis (Zhang et al., 2015) indicated reduced chemical weathering and sedimentation rates
513 precisely at the SSB, at least locally. These proxies were interpreted as a cooling episode whose
514 timing brings additional support for a diachronous onset of the cooling across latitude, spanning the
515 entire latest Smithian *G. sinuatum* Zone. Moreover, the abrupt shape of the positive CIE documented
516 by these authors conforms to that of most SSB shelf records in south China and in the northern
517 Indian margin. This suggests again the presence of a gap intercalated between the *G. sinuatum* Zone
518 and basal Spathian in the low latitudes. Hence, the late Smithian gap is apparently of global
519 significance but started earlier in the Boreal records. On the other hand, the deep sea pelagic SSB
520 record from the Panthalassic and near equatorial Mino Tamba Terrane highlights that both limbs and
521 maximum of the positive CIE are all gradual (Sakuma et al., 2012). This argues against a substantial
522 hiatus in sedimentation in the deep oceanic record. The age model constructed by these authors is
523 based on the correlation of their deep sea $\delta^{13}C_{org}$ record with the well dated, but incomplete $\delta^{13}C_{carb}$
524 shelf records from South China. They inferred that sedimentation rate increased by an order of

525 magnitude during the late Smithian. However, they placed their middle-late Smithian boundary at
526 the minimum of the negative CIE that is diagnostic of the middle Smithian. With the additional
527 problem of large error bars on dates and correlations, the late Smithian cannot be distinguished from
528 the middle Smithian in terms of sedimentation rate in this deep oceanic record. This rare deep sea
529 $\delta^{13}C_{org}$ record nevertheless reveals that most of the interval with elevated sedimentation rate is in
530 fact within the middle Smithian, in agreement with the shelf records from South China (e.g. Galfetti
531 et al., 2007b).

532 Whatever the respective efficiency and share of potential CO_2 sinks that may contribute to the
533 positive CIE (biological pump, buffering by marine carbonate - see Donnadieu et al. 2011; Jones et al.,
534 2016), their cumulated effects may still be insufficient for bringing down the pCO_2 to the level where
535 terrestrial ice can start forming at the poles. Temperature is also expected to closely track the carbon
536 budget if feedback mechanisms are preponderant. However, in the northern Indian margin the delay
537 of the temperature decrease (Goudemand et al., 2019) with respect to the earlier inception of the
538 positive CIE and black shales deposition amounts to the duration of the early late Smithian *W. tardus*
539 Zone. This delayed cooling suggests that some other primary mechanisms distinct from the feed back
540 processes must have come into play. A decrease in global volcanism near the middle-late Smithian
541 boundary is one potential explanation for this delay.

542 The Wallenbergfjellet section confirms that when preserved, the end of the positive CIE is of basal
543 Spathian age and follows a gentle pot-bellied shape without abrupt jumps akin to that of deep sea
544 records. The precise shape of the positive CIE is dictated by the distribution of gaps, sedimentation
545 rates, and sample spacing. If the maximum of the CIE is erased by a gap, the correlation of any
546 isotopic peak can be misleading in the absence of independent age control.

547 The mercury record from the Wallenbergfjellet section is worthy of particular attention, as it is the
548 only current record across the SSB where TOC concentrations are regularly above 1 wt.%. This means
549 that any changes in Hg/TOC ratios cannot be due to errors induced by low Hg or TOC concentrations.

550 The abrupt change from anomalously high Hg/TOC values in the Smithian to low levels in the
551 Spathian (Figure 4) could be interpreted as a switch from elevated volcanism to little or background
552 volcanic activity. However, this section differs from other published Hg/TOC anomalies of purported
553 volcanic origin in that the elevated Hg/TOC values observed in the middle Smithian are moderate in
554 magnitude, protracted (>18 m of section), and not accompanied by increased Hg concentrations
555 (Figure 4). It is therefore important to consider alternative non-volcanic possibilities for changes in
556 Hg/TOC concentrations.

557 Terrestrial and marine ecosystems are inherently different, leading to variations in nutrient cycling
558 and thereby influencing the degree of Hg enrichments in various organic carbon reservoirs. Therefore,
559 changes to the dominant source of organic matter could result in variations in Hg/TOC values,
560 creating false Hg/TOC 'anomalies'. At present, potential differences in Hg/TOC values between
561 terrestrial and marine sources are poorly understood, as there is a huge range of ecosystems in each
562 realm that each have differing Hg-uptake pathways. There is some limited evidence to suggest that
563 terrestrially derived sediments have higher background Hg/TOC values than fully marine sediments
564 (Percival et al., 2015; 2017). This is corroborated with an apparent correlation of Hg/TOC anomalies
565 with distance to shore from studies of the latest Triassic and early Toarcian, although it is unclear
566 whether this represents higher Hg/TOC values in organic matter or another source such as clay
567 minerals (Them II et al., 2019).

568 In this study, the increase in hydrogen index at the SSB in our data set could be caused by decreased
569 oxidation and bioturbation, or by a shift to a dominance of marine organic matter. With the latter
570 interpretation, the close correlation with Hg/TOC anomalies and terrestrially-sourced organic matter
571 could be a cause for part or perhaps all of the step change in Hg/TOC values observed across the SSB
572 in our data set (Figure 5B). The smaller Hg/TOC anomalies observed in this study compared to those
573 observed at Festningen (Grasby et al., 2016) may support the hypothesis of Them II et al. (2019) that
574 the magnitude of Hg/TOC anomalies are often positively correlated with proximity to paleoshoreline,

575 although the relatively high TOC concentrations throughout the section would suggest this is due to
576 higher Hg/TOC values of terrestrially derived organic matter rather than adsorption onto clay
577 surfaces.

578 Redox conditions are also critical to the dominant mode of Hg deposition (Them II et al., 2019), as a
579 recent study from the Ordovician/Silurian boundary showed that Hg concentrations are governed by
580 the prevalence of pyrite rather than organic matter under euxinic conditions (Shen et al., 2019b). The
581 close correlation between Hg and Fe in the Wallenbergfjellet section (Figure 4; 5D) might suggest
582 that Hg may indeed be partially associated with pyrite instead of organic matter. However, the clear
583 change in hydrogen index between the Smithian and the Spathian (Figure 5B) could be a result of
584 decreased oxidization of organic matter, thus suggesting the Spathian is the more anoxic
585 environment. Moreover, Fe is ubiquitous in the Smithian Lusitaniadalen Member with minor
586 occurrences of pyrite, while Fe is largely restricted to common framboidal pyrite in the Spathian
587 Vendomdalen Member (Figure 6). If Hg was dominantly deposited by sulfides, then one would expect
588 Hg/TOC ratios to be elevated in more anoxic strata, the opposite of what is observed across the SSB.
589 Based on the data available, it therefore appears that sulfide deposition is not a controlling factor in
590 variations to Hg/TOC anomalies when comparing Smithian and Spathian strata. However, there is
591 clearly a correlation between Hg and Fe within the Spathian.

592 The scale and prolonged nature of the Hg/TOC anomalies in the middle Smithian are indicative of
593 two mutually inclusive possibilities: 1) that terrestrial ecosystems in the Early Triassic have inherently
594 higher Hg/TOC ratios than marine ecosystems; and/or 2) there was a sustained global Hg-enrichment
595 that disproportionately affected the terrestrial realm. The magnitude of this protracted anomaly
596 would suggest that elevated global volcanism, possibly from renewed activity from the Siberian Traps,
597 is a plausible explanation. What is less clear is whether the low Hg/TOC concentrations observed in
598 the early Spathian are due to a cessation of environmental Hg-enrichment, a change in organic
599 matter source with Hg-enrichments limited to the terrestrial realm, or a combination thereof.

600 Unfortunately, there is little information on organic matter type at previously reported localities with
601 Hg/TOC anomalies near the SSB (Arctic Canada and western Spitsbergen). There is also a substantial
602 temporal offset (i.e. the *W. tardus* Zone) between the peak in Hg/TOC anomalies and the climax of
603 the marine extinction at the SSB, challenging the hypothesis that volcanic degassing is the cause of
604 the environmental crises at the SSB.

605

606 **6. Conclusions**

607 Middle -not late- Smithian times witnessed a thermal maximum as suggested by oxygen isotopic
608 composition, rates of chemical weathering, biogeography of conodonts and the presence of a spore
609 spike. Nektonic organisms responded to these adverse conditions by producing many short-lived
610 species, as exemplified by the northern Indian margin ammonoid record (Brühwiler et al., 2010,
611 Bucher et al. 2013). The extinction of the ammonoids and conodonts clearly post dates the middle
612 Smithian thermal maximum and is intimately associated with a global gap at or close to the SSB and a
613 late Smithian cooler and dryer climate. The Early Triassic Hg/TOC anomaly previously documented in
614 Spitsbergen is here shown to be of middle Smithian age (*E. romunderi* Zone), thus questioning the
615 role of volcanism as a trigger for the late Smithian extinctions and the commonly associated “lethally”
616 hot scenario. A slight decrease in the Hg/TOC values is seen already in the late Smithian *W. tardus*
617 Zone, coeval with or slightly predating the positive carbon isotope excursion marking the
618 Smithian/Spathian boundary. Hg/TOC values then remain low through the Spathian.

619 The cause of this Smithian Hg/TOC anomaly is not fully resolved. Errors induced by low Hg or TOC
620 values that affect other SSB localities can be discounted for this section due to sufficiently high (>0.5
621 wt.%) TOC concentrations. Redox proxies suggest less oxygenated conditions coinciding with low
622 Hg/TOC ratios in the Spathian, which indicates that Hg deposition by sulfides is not a controlling
623 factor in the difference between Smithian and Spathian strata. Crucially at Wallenbergfjellet, the
624 termination of the elevated Hg/TOC values coincides with a shift in the hydrogen index, which can be

interpreted as a change from predominantly terrestrial to marine organic matter (although a decrease in oxidation is an alternative explanation). This suggests that it is possible that a change in the supply of organic matter from more terrestrial to more marine source may account for the observed differences in Hg/TOC values from the Smithian to the Spathian. This could be due to more efficient Hg-uptake in terrestrial ecosystems than marine environments at this time, and/or that there was an elevated Hg source to the environment, such as volcanism, that preferentially impacted the terrestrial realm. The former scenario does not require elevated volcanism from the Siberian Traps or elsewhere to account for the observed Hg/TOC record at Wallenbergfjellet, highlighting the need for caution when interpreting Hg/TOC anomalies in the Early Triassic (and potentially other time periods) as a signal of volcanism.

Acknowledgments

We are grateful to Franz-Josef Lindemann for invaluable help with the field work. The Swiss SNF (project 200020-160055) supported field and lab work of HB and ESH. MTJ is supported by the Research Council of Norway through its Centers of Excellence funding scheme, project number 223272, and the Research Council of Norway Unge Forskertalenter project 'Ashlantic', project number 263000. Stephen Crowley, Liverpool University, carried out the isotope analyses. Eirini Zacharaki, Natural History Museum, Oslo, assisted with SEM-EDX imaging. Tamsin Mather and Lawrence Percival are thanked for their help and assistance. We are highly grateful for constructive comments by Jun Shen, Thomas Algeo, and an anonymous reviewer.

References

647 Baresel, B., Bucher, H., Brosse, M., Cordey, F., Guodun, K. and Schaltegger, U. 2017. Precise age for
648 the Permian–Triassic boundary in South China from high precision U-Pb geochronology and Bayesian
649 age–depth modeling. *Solid Earth* 8, 361–378.

650 Baud, A., Magaritz, M., Holser, W.T., 1989. Permian-Triassic of the Tethys: Carbon isotope studies.
651 *Geologische Rundschau* 78, 649–677.

652 Black, B.A., Elkins-Tanton, L.T., Rowe,M.C., Peate, I.U., 2012. Magnitude and consequences of volatile
653 release from the Siberian Traps. *Earth and Planetary Science Lett*ers 317–318, 363–373.

654 Black, B.A., Lamarque, J.-F., Shields, C.A., Elkins-Tanton, L.T., Kiehl, J.T., 2014. Acid rain and ozone
655 depletion from pulsed Siberian Traps magmatism. *Geology* 42, 67–70.

656 Bin, C., Xiaoru, W., Lee, F.S.C., 2001. Pyrolysis coupled with atomic absorption spectrometry for the
657 determination of mercury in Chinese medicinal materials. *Analytica Chimica Acta* 447, 161–169.

658 Bower, J., Savage, K.S., Weinman, B., Barnett, M.O., Hamilton, W.P., Harper, W.F., 2008.
659 Immobilization of mercury by pyrite (FeS_2). *Environmental Pollution* 156, 504–514.

660 Brayard, A., Bucher, H., Escarguel, G., Fluteau, F., Bourquin, S., Galfetti, T. 2006. The Early Triassic
661 ammonoid recovery: Paleoclimatic significance of diversity gradients. *Palaeogeography,*
662 *Palaeoclimatology, Palaeoecology* 239, 374–95.

663 Brayard, A., Bucher, H. 2008. Smithian (Early Triassic) ammonoid faunas from northwestern Guangxi
664 (South China): Taxonomy and Biochronology. *Fossils and Strata 55*, 179 pp.

665 Brayard, A., Bucher, H. 2015. Permian-Triassic extinctions and rediversifications. In: C. Klug *et al*.
666 (eds.), Ammonoid Paleobiology: From macroevolution to paleogeography. *Topics in Geobiology 44*,
667 DOI 10.1007/978-94-017-9633-0_17.

668 Brayard, A., Escarguel, G., Bucher, H., Monnet, C., Brühwiler, T., Goudemand, N., Galfetti, T., Guex, J.
669 2009. Good genes and good luck: Ammonoid diversity and the end-Permian mass extinction. *Science*
670 325, 1118–1121.

671 Brühwiler, T., Bucher, H., Brayard, A., Goudemand, N. 2010. High-resolution biochronology and
672 diversity dynamics of the Early Triassic ammonoid recovery: the Smithian faunas of the Northern
673 Indian Margin. *Palaeogeography, Palaeoclimatology, Palaeoecology* 297, 491–501.

674 Bucher, H., Hochuli, P.A., Goudemand, N., Schneebeli-Hermann, E., Romano, C., Hautmann, M.,
675 Hofmann, R., Brayard, A., Vennemann, T., Weissert, H. 2013. Some like it hot: The Smithian
676 diversification-extinction model. *GSA Abstracts with Programs* 45, 883.

677 Burgess, S.D., Bowring, S., Shen, S.-z., 2014. High-precision timeline for Earth's most severe extinction.
678 *Proceedings of the National Academy of Science, USA* 111, 3316–3321.
679 http://dx.doi.org/10.1073/pnas.1317692111.

680 Burgess, S.D., Bowring, S.A. 2015. High-precision geochronology confirms voluminous magmatism
681 before, during, and after Earth's most severe extinction. *Science Advances* 1, e1500470.

682 Craig, H.S. 1957. Isotopic standards for carbon and oxygen and correction factors for mass-
683 spectrometric analysis of carbon dioxide. *Geochemica et Cosmochimica Acta* 12, 133–149.

684 Dagys, A.S. 1994. Lower Triassic stage, substage and zonal scheme of north-eastern Asia. In: Guex, J.,
685 Baud, A. (eds) Recent developments on Triassic stratigraphy. *Mémoires de Geologie (Lausanne)* 22,
686 15–23.

687 Donnadieu, Y., Dromart, G., Goddéris, Y., Pucéat, E., Brigaud, B., Dera, G., Dumas, C., Olivier, N. 2011.
688 A mechanism for brief glacial episodes in the Mesozoic greenhouse. *Paleoceanography* 26, PA3212.

689 Duan, Y., Han, D.S., Batchelor, B., Abdel-Wahab, A., 2016. Synthesis, characterization, and application
690 of pyrite for removal of mercury. *Colloids and Surfaces A: Physicochemical and Engineering Aspects*
691 490, 326–335.

692 Durand, B., Monin, J.C. 1980. Elemental analysis of kerogens (C, H, O, N, S, Fe). Pp. 113-142, In
693 Durand, B. (ed.): Kerogen – insoluble organic matter from sedimentary rocks. Éditions Technip, Paris.

694 Dypvik, H., Harris, N.B. 2001. Geochemical facies analysis of fine-grained siliciclastics using Th/U,
695 Zr/Rb and (Zr+Rb)/Sr ratios. *Chemical Geology* 181, 131–146.

696 Ernst, R.E., Youbi, N. 2017. How large igneous provinces affect global climate, sometimes cause mass
697 extinctions, and represent natural markers in the geological record. *Palaeogeography*
698 *Palaeoclimatology, Palaeoecology* 478, 30–52.

699 Font, E., Adatte, T., Sial, A.N., Lacerda, L.D., Keller, G., Punekar, J., 2016. Mercury anomaly, Deccan
700 volcanism, and the end-Cretaceous mass extinction. *Geology* 44, 171–174.

701 Frazer, J.W., Crawford, R. 1963. Modifications in the simultaneous determination of carbon,
702 hydrogen, and nitrogen. *Mikrochimica Acta* 51, 561–566.

703 Galfetti, T., Hochuli, P.A., Brayard, A. Bucher, H., Weissert, H., Vigran, J.O. 2007a. Smithian-Spathian
704 boundary event: Evidence for global climatic change in the wake of the end-Permian biotic crisis.
705 *Geology* 35, 291-294. doi: 10.1130/G23117A

706 Galfetti, T., Bucher, H., Ovtcharova, M., Schaltegger, U., Brayard, A., Brühwiler T., Goudemand, N.,
707 Weissert H., Hochuli, P., Cordey, F., Guodon K. 2007b. Timing of the Early Triassic carbon cycle
708 perturbations inferred from new U-Pb ages and ammonoid biochronozones. *Earth and Planetary*
709 *Science Letters* 258, 593–604.

710 Golonka, J., 2011. Phanerozoic palaeoenvironment and palaeolithofacies maps of the Arctic region. In
711 Spencer, A.M., Embry, A.F., Gautier, D.L., Stoupakova, A.V., Sørensen, K. (eds.), Arctic Petroleum
712 Geology. *Geological Society, London, Memoirs*, 35, 79-129, doi: 10.1144/M35.6.

713 Goudemand, N., Orchard, M.J., Tafforeau, P., Urdy, S., Brühwiler, T., Brayard, A., Galfetti, T., Bucher,
714 H. 2012. Early Triassic conodont clusters from South China: Revision of the architecture of the 15
715 element apparatuses of the superfamily Gondolelloidea. *Palaeontology* 55, 1021–1034.

716 Goudemand, N., Romano, C., Brayard, A., Hochuli, P.A., Bucher, H. 2013. Comment on "Lethally hot
717 temperatures during the Early Triassic greenhouse". S*cience* 339 (6123), 1033.

718 Goudemand, N., Romano, C., Leu, M., Bucher, H., Trotter, J., Williams, I. 2019. Dynamic interplay
719 between climate and marine biodiversity upheavals during the Early Triassic Smithian–Spathian biotic
720 crisis. *Earth Science Reviews*, https://doi.org/10.1016/j.earscirev.2019.01.01

721 Grasby, S.E., Sanei, H., Beauchamp, B., Chen, Z. 2013. Mercury deposition through the Permo-Triassic
722 biotic crisis. *Chemical Geology* 351, 209–216.

723 Grasby, S.E., Beauchamp, B., Bond, D.P.G., Wignall, P.B., Sanei, H. 2016. Mercury anomalies
724 associated with three extinction events (Capitanian Crisis, Latest Permian Extinction and the
725 Smithian/Spathian Extinction) in NW Pangea. *Geological Magazine* 153, 285–297.

726 Hammer, Ø., Harper, D.A.T., Ryan, P.D. 2001. PAST: Paleontological Statistics software package for
727 education and data analysis. *Palaeontologia Electronica* 4(1), 9 pp.

728 Hardisty, D.S., Lyons, T.W., Riedinger, N., Isson, T.T., Owens, J.D., Aller, R.C., Rye, D.M., Planavsky,
729 N.J., Reinhard, C.T., Gill, B.C., Masterson, A.L., Asael, D., Johnston, D.T. 2018. An evaluation of
730 sedimentary molybdenum and iron as proxies for pore fluid paleoredox conditions. *American Journal*
731 *of Science* 318, 527–556.

732 Hautmann, M. 2014. Diversification and diversity partitioning. *Paleobiology* 40, 162–176.

733 Hautmann, M., Bagherpour, B., Brosse, M., Frisk, Å., Hofmann, R., Baud, A., Nützel, Goudemand, N.,
734 Bucher, H. 2015. Competition in slow motion: The unusual case of benthic marine communities in the
735 wake of the end-Permian mass extinction. *Palaeontology* 58, 871–901. doi: 10.1111/pala.12186

736 Hermann, E., Hochuli, P.A., Bucher, H., Brühwiler, T., Hautmann, M., Ware, D., Roohi, G. 2011.
737 Terrestrial ecosystems on North Gondwana in the aftermath of the end-Permian mass extinction.
738 *Gondwana Research* 20, 630–637.

739 Hochuli, P.A., Sanson-Barrera, A., Schneebeli-Hermann, E., Bucher, H. 2016. Severest crisis
740 overlooked - Worst disruption of terrestrial environments postdates the Permian-Triassic mass
741 extinction. *Nature Scientific Reports*. DOI: 10.1038/srep28372

742 Hubred, J.H. 2006. Thermal effects of basaltic sill emplacement in source rocks on maturation and
743 hydrocarbon generation. Cand. Scient. Thesis, University of Oslo. Permanent link:
744 http://urn.nb.no/URN:NBN:no-12609.

745 Jattiot, R., Bucher, H., Brayard, A., Monnet, C., Jenks J.F., Hautmann, M. 2015. Revison of the genus
746 *Anasibirites* Mojsisovics. 1896 (Ammonoidea): An iconic and cosmopolitan taxon of the late Smithian
747 (Early Triassic) extinction. *Papers in Palaeontology*. DOI: 10.1002/spp2.1036.

748 Jattiot, R., Bucher, H., Brayard, A., Brosse, M., Jenks, J.F., Bylund, K.G. 2017. Smithian ammonoid
749 faunas from northeastern Nevada: implications for Early Triassic biostratigraphy and correlation
750 within the western USA basin. *Palaeontographica Abteilung A* 309, 1–89.

751 Jenks, J.F., Brayard, A. 2018. Smithian (Early Triassic) ammonoids from Crittenden Springs, Elko
752 County, Nevada: taxonomy, biostratigraphy and biogeography. *New Mexico Museum of Natural*
753 *History & Science Bulletin* 78, 175 pp.

754 Jones, M.T., Jerram, D.A., Svensen, H.H., Grove, C. 2016. The effects of large igneous provinces on the
755 global carbon and sulphur cycles. *Palaeogeography Palaeoclimatology Palaeoecology* 441, 4–21.

Jones, M.T., Percival, L.M.E., Stokke, E.W., Frieling, J., Mather, T.A., Riber, L., Schubert, B.A., Schultz, B., Tegner, C., Planke, S., Svensen, H.H., 2019. Mercury anomalies across the Palaeocene-Eocene Thermal Maximum. *Climate of the Past* 15, 1-20, doi:10.5194/cp-15-1-2019.

Kamo, S.L., Czamanske, G.K., Amelin, Y., Fedorenko, V.A., Davis, D.W., Trofimov, V.R., 2003. Rapid eruption of Siberian flood-volcanic rocks and evidence for coincidence with the Permian-Triassic boundary and mass extinction at 251 Ma. *Earth and Planetary Science Letters* 214, 75–91, doi:10.1016/S0012-821X(03)00347-9.

Keller, G., Mateo, P., Punekar, J., Khozyem, H., Gertsch, B., Spangenberg, J., Bitchong, A., Adatte, T., 2018. Environmental changes during the cretaceous-Paleogene mass extinction and Paleocene-Eocene thermal maximum: Implications for the Anthropocene. *Gondwana Research* 56, 69–89, doi:10.1016/j.gr.2017.12.002.

Komatsu, T., Takashima, R., Shigeta, Y., Maekawa, T., Tran, H.D., Cong, T.D., Sakata, S., Dinh, H.D., Takahashi, O. 2016. Carbon isotopic excursions and detailed ammonoid and conodont biostratigraphies around Smithian–Spathian boundary in the Bac Thuy Formation, Vietnam. *Palaeogeography, Palaeoclimatology, Palaeoecology* 454, 65–74.

Leu, M., Bucher, H., Goudemand, N. 2018. Clade-dependent size response of conodonts to environmental changes during the late Smithian extinction. *Earth-Science Reviews*, https://doi.org/10.1016/j.earscirev.2018.11.003

Lucas, S.G. 2018. The GSSP method of chronostratigraphy: A critical review. *Frontiers in Earth Science*, https://doi.org/10.3389/feart.2018.00191

Magaritz, M., Bart, R., Baud, A., Holser, W.T., 1988. The carbon-isotope shift at the Permian/Triassic boundary in the southern Alps is gradual. *Nature* 331, 337–339.

778 Major, H., Haremo, P., Dallmann, W.K., Andresen, A., 2001. Geological Map of Svalbard 1:100,000
779 Sheet C9G Adventdalen (Norsk Polarinstitutt Temakart, www.npolar.no).

780 Meyer, K.M., Yu, M., Jost, A.B., Kelly, B.M., Payne, J.L., 2011. $\delta^{13}C$ evidence that high primary
781 productivity delayed recovery from end-Permain mass extinction. *Earth and Planetary Science Letters*
782 302, 378–384.

783 Mørk, A., Knarud, R., Worsley, D. 1982. Depositional and diagenetic environments of the Triassic and
784 Lower Jurassic succession of Svalbard. In: *Arctic Geology and Geophysics* (eds. A.F. Embry, H.R.
785 Balkwill), pp. 371–398. Canadian Society of Petroleum Geologists Memoir 8.

786 Mørk, A., Elvebakk, G., Forsberg, A.W., Hounslow, M.W., Nakrem, H.A., Vigran, J.O., Weitschat, W.
787 1999. The type section of the Vikinghøgda Formation: a new Lower Triassic unit in central and
788 eastern Svalbard. *Polar Research* 18, 51–82.

789 Orchard, M.J. 2007. Conodont diversity and evolution through the latest Permian and Early Triassic
790 upheavals. *Palaeogeography, Palaeoclimatology, Palaeoecology* 252, 93–117.

791 Orchard, M.J., Zonneveld, J.-P. 2009. The Lower Triassic Sulphur Mountain Formation in the Wapiti
792 Lake area: lithostratigraphy, conodont biostratigraphy, and a new biozonation for the lower
793 Olenekian (Smithian). *Canadian Journal of Earth Sciences* 46, 757–790.

794 Outridge, P.M., Sanei, H., Stern, G.A., Hamilton, P.B., Goodarzi, F., 2007. Evidence for control of
795 mercury accumulation rates in Canadian High Arctic lake sediments by variations of aquatic primary
796 productivity. *Environmental Science & Technology* 41, 5259–5265.

797 Ovtcharova, M., Goudemand, N., Hammer, Ø., Guodun, K., Cordey, F., Galfetti , T., Schaltegger, U.,
798 Bucher, H. 2015. Developing a strategy for accurate definition of a geological boundary through
799 radio-isotopic and biochronological dating: the Early–Middle Triassic boundary (South China). *Earth-*
800 *Science Reviews* 146, 65–76.

801 Paton, M.T., Ivanov, A.V., Fiorentini, M.LK., McNaughton, N.J., Mudrovska, I., Reznitskii, L.Z.,
802 Demonterova, E.I. 2010. Late Permian and Early Triassic magmatic pulses in the Angara-Taseeva
803 syncline, Southern Siberian Traps and their possible influence on the environment. *Russian Geology*
804 *and Geophysics* 51, 1012–1020.

805 Payne, J.L., Lehrmann, D.J., Wei, J., Orchard, M.J., Schrag, D.P., Knoll, A.H., 2004. Large perturbations
806 of the carbon cycle during recovery from the end-Permian extinction. *Science* 305, 506–509.

807 Percival, L.M.E., Witt, M., Mather, T., Hermoso, M., Jenkyns, H., Hesselbo, S., Al-Suwaidi, A., Storm,
808 M., Xu, W., Ruhl, M., 2015. Globally enhanced mercury deposition during the end-Pliensbachian
809 extinction and Toarcian OAE: A link to the Karoo-Ferrar Large Igneous Province. *Earth and Planetary*
810 *Science Letters* 428, 267–280.

811 Percival, L.M.E., Ruhl, M., Hesselbo, S.P., Jenkyns, H.C., Mather, T.A., Whiteside, J.H., 2017. Mercury
812 evidence for pulsed volcanism during the end-Triassic mass extinction. *Proceedings of the National*
813 *Academy of Sciences* 114, 7929-7934, doi: 10.1073/pnas.1705378114.

814 Percival, L.M.E., Jenkyns, H.C., Mather, T.A., Dickson, A.J., Batenburg, S.J., Ruhl, M., Hesselbo, S.P.,
815 Barclay, R., Jarvis, I., Robinson, S.A., Woelders, L., 2018. Does large igneous province volcanism
816 always perturb the mercury cycle? Comparing the records of Oceanic Anoxic Event 2 and the end-
817 Cretaceous to other Mesozoic events. *American Journal of Science* 318, 799–860,
818 doi:10.2475/08.2018.01.

819 Pyle, D.M., Mather, T.A., 2003. The importance of volcanic emissions for global atmospheric mercury
820 cycle. *Atmospheric Environment* 37, 5115–5124.

821 Ravichandran, M., 2004. Interactions between mercury and dissolved organic matter—a review.
822 *Chemosphere* 55, 319–331.

823 Romano, C., Goudemand, N., Vennemann, T.W., Ware, D., Schneebeli-Hermann, E., Hochuli, P.A.,
824 Brühwiler, T., Brinkmann, W., Bucher, H. 2013. Climate and biotic upheavals following the end-
825 Permian mass extinction. *Nature Geoscience* 6, 57–60.

826 Ruiz, W.L.G., Tomiyasu, T., 2015. Distribution of mercury in sediments from Kagoshima Bay, Japan,
827 and its relationship with physical and chemical factors. *Environmental Earth Sciences* 74, 1175–1188.

828 Sakuma, H., Tada, R., Ikeda, M., Kashiyama, Y., Ohkouchi, N., Ogawa, N.O., Watanabe, S., Tajika, E.,
829 Yamamoto, S., 2012. High-resolution lithostratigraphy and organic carbon isotope stratigraphy of the
830 Lower Triassic pelagic sequence in central Japan. *Island Arc* 21, 79–100.

831 Sanei, H., Grasby, S., Beauchamp, B., 2012. Latest Permian mercury anomalies. *Geology* 40, 63–66.

832 Sanei, H., Outridge, P.M., Stern, G.A., MacDonald, R.W., 2014. Classification of mercury-labile organic
833 matter relationships in lake sediments. *Chemical Geology* 373, 87–92.

834 Scheyer, T.M., Romano, C., Jenks, J., Bucher, H. 2014. Early Triassic marine biotic recovery: The
835 predators' perspective. *PLoS One*, DOI: 10.1371/journal.pone.0088987.

836 Schovsbo, N.H., Nielsen, A.T., Harstad, A.O., Bruton. D.L. 2018. Stratigraphy and geochemical
837 composition of the Cambrian Alum Shale Formation in the Porsgrunn core, Skien-Langesund district,
838 southern Norway. *Bulletin of the Geological Society of Denmark* 66, 1–20.

839 Selin, N.E., 2009. Global biogeochemical cycling of mercury: a review. *Annual Review of Environment*
840 *and Resources* 34, 43–63.

841 Sepkoski Jr., J.J., 1996. Patterns of Phanerozoic extinction: A perspective from global databases, in
842 Walliser, O.H., ed., Global Events and Event Stratigraphy in the Phanerozoic: Berlin, Springer-Verlag,
843 35–51.

844 Sepkoski Jr., J.J., 2002. A compendium of fossil marine animal genera. *Bulletins of American*
845 *Paleontology* 363, 1–560.

846 Shen, J., Algeo, T.J., Hu, Q., Zhang, N., Zhoul, L., Xia, W., Xie, S., Feng, Q. 2012. Negative C-isotope
847 excursions at the Permian-Triassic boundary linked to volcanism. *Geology* 40, 963–966.

848 Shen, J., Algeo, T.J., Planavsky, N.J., Yu, J.X., Feng, Q.L., Song, H.J., Song, H.Y., Rowe, H., Zhou, L.,
849 Chen, J.B. 2019a. Mercury enrichments provide evidence of Early Triassic volcanism following the
850 end-Permian mass extinction. *Earth-Science Reviews*, accepted.

851 Shen, J., Algeo, T.J., Chen, J.B., Planavsky, N.J., Feng, Q.L., Yu, J.X., Liu, J.L. 2019b. Mercury in marine
852 Ordovician-Silurian boundary sections of South China is sulfide-hosted and non-volcanic in origin.
853 *Earth and Planetary Science Letters* 511, 130–140.

854 Sial, A., Lacerda, L., Ferreira, V., Frei, R., Marquillas, R., Barbosa, J., Gaucher, C., Windmöller, C.,
855 Pereira, N., 2013. Mercury as a proxy for volcanic activity during extreme environmental turnover:
856 The Cretaceous-Paleogene transition. *Palaeogeography Palaeoclimatology Palaeoecology* 387, 153–
857 164.

858 Sofer, Z. 1980. Preparation of carbon dioxide for stable carbon isotope analysis of petroleum
859 fractions. *Analytical Chemistry* 52, 1389–1391.

860 Song, H.Y., Tong, J., Algeo, T.J., Horacek, M., Qiu, H., Song, H.J., Tian, L., Chen, Z.-Q. 2013. Large
861 vertical $\delta^{13}C_{DIC}$ gradients in Early Triassic seas of the South China craton: Implications for
862 oceanographic changes related to Siberian Traps volcanism. *Global and Planetary Change* 105, 7–20.

863 Sun, Y., Joachimski, M.M., Wignall, P.B., Yan, C., Chen, Y., Jiang, H., Wang, L., Lai X., 2012. Lethally hot
864 temperatures during the early Triassic greenhouse. *Science* 338, 366-370.

865 Svensen, H., Planke, S., Polozov, A.G., Schmidbauer, N., Corfu, F., Podladchikov, Y.Y., Jamtveit, B.,
866 2009. Siberian gas venting and the end-Permian environmental crisis. *Earth and Planetary Science*
867 *Letters* 277, 490–500.

868 Them II, T.R., Jagoe, C.H., Caruthers, A.H., Gill, B.C., Grasby, S.E., Gröcke, D.R., Yin, R., Owens, J.D.,
869 2019. Terrestrial sources as the primary delivery mechanism of mercury to the oceans across the

870 Toarcian Oceanic Anoxic Event (Early Jurassic). *Earth and Planetary Science Letters* 507, 62–72,
871 doi:10.1016/j.epsl.2018.11.029.

872 Thibodeau, A.M., Ritterbush, K., Yager, J.A., West, A.J., Ibarra, Y., Bottjer, D.J., Berelson, W.M.,
873 Bergquist, B.A., and Corsetti, F.A., 2016. Mercury anomalies and the timing of biotic recovery
874 following the end-Triassic mass extinction. *Nature Communications* 7, 11147.

875 Tong, J.,. Zhang, S., Zuo, J., Xiong, X. 2007. Events during Early Triassic recovery from the end-Permian
876 extinction. *Global and Planetary Change* 55, 66–80.

877 Torsvik, T.H., Cocks, L.R.M., 2017. Earth History and Palaeogeography. *Cambridge University Press*,
878 317 pp., ISBN: 978-1-107-10532-4.

879 Tozer, E.T. 1967. A standard for Triasssic time. *Geological Survey of Canada Bulletin* 156, 103 p.

880 Tozer, E.T. 1994. Canadian Triassic ammonoid faunas. *Geological Survey of Canada Bulletin* 467, 1–
881 663.

882 Tribovillard, N., Algeo, T.J., Lyons, T., Riboulleau, A. 2006. Trace metals as paleoredox and
883 paleoproductivity proxies: An update. *Chemical Geology* 232, 12–32.

884 Wang, X., Cawood, P.A., Zhao, H., Zhao, L., Grasby, S.E., Chen, Z.-Q., Zhang, L. 2019. Global mercury
885 cycle during the end-Permian mass extinction and subsequent Early Triassic recovery. *Earth and*
886 *Planetary Science Letters 513*, 144–155.

887 Wignall, P.B., Bond, D.P.G., Sun, Y., Grasby, S.E., Beauchamp, B., Joachimski, M.M., Blomeier, D.P.G.
888 2016. Ultra-shallow marine anoxia in an Early Triassic shallow-marine clastic ramp (Spitsbergen) and
889 the suppression of benthic radiation. *Geological Magazine* 153, 316–331.

890 Xie, S., Pancost, R.D., Wang, Y., Yang, H., Wignall, P.B., Luo, G., Jia, C., Chen, L., 2010. Cyanobacterial
891 blooms tied to volcanism during the 5 m.y. Permo–Triassic biotic crisis. *Geology* 38, 447–450.

892 Zhang, L., Zhao, L., Chen, Z.-Q., Algeo, T.J., Li, Y., Cao, L. 2015. Amelioration of marine environments
893 at the Smithian-Spathian boundary, Early Triassic. *Biogeosciences* 12, 1597–1613.

894 Zhang, L., Orchard, M.J., Brayard, A., Algeo, T.J., Zhao, L., Chen, Z.-Q., Lyu, Z. 2019. The
895 Smithian/Spathian boundary (late Early Triassic): A review of ammonoid, conodont, and carbon-
896 isotopic criteria. *Earth-Science Reviews*, https://doi.org/10.1016/j.earscirev.2019.02.014